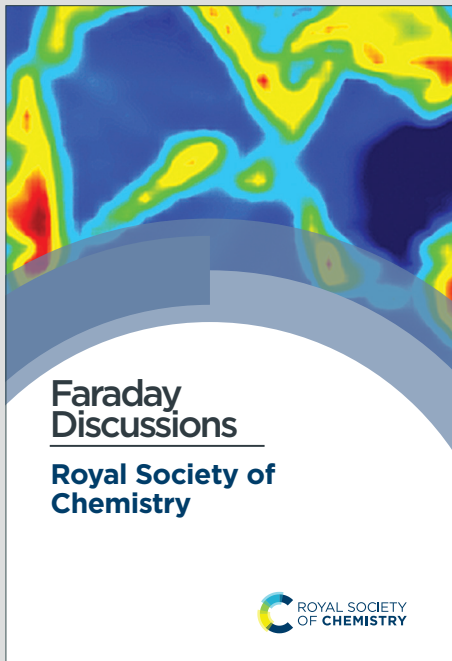


Faraday Discussions

Accepted Manuscript



This is an Accepted Manuscript, which has been through the Royal Society of Chemistry peer review process and has been accepted for publication.

Accepted Manuscripts are published online shortly after acceptance, before technical editing, formatting and proof reading. Using this free service, authors can make their results available to the community, in citable form, before we publish the edited article. We will replace this Accepted Manuscript with the edited and formatted Advance Article as soon as it is available.

You can find more information about Accepted Manuscripts in the [Information for Authors](#).

Please note that technical editing may introduce minor changes to the text and/or graphics, which may alter content. The journal's standard [Terms & Conditions](#) and the [Ethical guidelines](#) still apply. In no event shall the Royal Society of Chemistry be held responsible for any errors or omissions in this Accepted Manuscript or any consequences arising from the use of any information it contains.

This article can be cited before page numbers have been issued, to do this please use: L. Rikanati, Y. Hovav and E. Gross, *Faraday Discuss.*, 2026, DOI: 10.1039/D5FD00139K.

IR Nanospectroscopy Mapping of Facet-Dependent Sulfur Poisoning and Thermal Regeneration on Platinum Nanocrystals

[View Article Online](#)

DOI: 10.1039/D5FD00139K

Lihi Rikanati, Yehonatan Hovav and Elad Gross*

Institute of Chemistry and The Center for Nanoscience and Nanotechnology, The Hebrew University, Jerusalem 91904, Israel

*Email: elad.gross@mail.huji.ac.il



Abstract

[View Article Online](#)

DOI: 10.1039/D5FD00139K

Sulfur poisoning critically limits the activity and durability of Pt catalysts, yet the nanoscale structure-reactivity relationships that govern sulfate adsorption and its thermal desorption remain poorly resolved. Using infrared nanospectroscopy, we directly map the spatial distribution, adsorption geometry, and temperature-dependent evolution of sulfate species on individual Pt nanocrystals (NCs) with well-defined facets. At room temperature, SO_x species preferentially accumulate at defect-rich inter-facet regions, edges, and open Pt(100)-like facets, in which bidentate adsorption dominates. Flat Pt(111) terraces exhibit lower SO_x coverage and a larger contribution from tridentate species. Mild annealing (50–200 °C) induces selective desorption from undercoordinated sites and drives a structural transition from bidentate to tridentate coordination as species migrate toward highly coordinated terrace regions. At 300 °C, most sulfate species desorb from edges and side facets, whereas thermally robust tridentate species persist at the NC interior. These results provide a facet-resolved picture of sulfur adsorption and regeneration pathways, revealing how local surface structure dictates the stability and thermal evolution of poisoning species on Pt catalysts.



Introduction

Catalyst poisoning results in deactivation caused by the strong and often irreversible adsorption of molecular or atomic species to active metal sites.¹ Sulfur-containing compounds (e.g., sulfuric acid and its derivatives), carbon monoxide, and halide ions are among the most potent poisoning agents.^{2,3} The consequences of surface poisoning include reduced catalytic efficiency, lower product yields, and, ultimately, the need for catalyst replacement or regeneration.^{3–5}

Poisons such as sulfur form strong bonds with Pt surface atoms, saturating active sites and preventing reactant adsorption. Chemical reactions between the poisoning species and the catalyst can also generate new surface compounds that may either desorb from the surface or further block catalytic sites.³ Strongly bound poisons, such as SO_x -Pt species, often require harsh treatments for removal and restoration of catalytic activity.^{3,6–8} Therefore, analyzing the adsorption and desorption patterns of SO_x species on Pt nanoparticles is essential for understanding the mechanisms of catalyst poisoning and guiding regeneration strategies.

The interaction between sulfuric acid and Pt depends strongly on the arrangement and coordination of the surface atoms and on the chemical properties of the SO_x species.⁹ Sulfate is mainly adsorbed in a bidentate or tridentate coordination modes and the adsorption geometry directly influences the adsorption strength and thermal stability of the poisoning species.^{10–12} On Pt(111), sulfate predominantly adopts a well-ordered, bidentate or tridentate geometry stabilized by the close-packed terrace arrangement.¹³ On Pt(100), which is characterized with higher density of bridge sites, sulfate binds more weakly and often in a tilted bidentate configuration.^{14,15}

The natural inter- and intra-particle structural heterogeneity of catalytic nanoparticles^{16–20} makes it challenging to directly probe how different surface sites influence SO_x poisoning and its removal. Resolving these site-dependent effects requires both experimental techniques capable of providing nanoscale chemical information and model catalysts with well-defined surface structures. Recent advances in high spatial resolution spectroscopy have enabled nanoscale investigations of catalytic nanoparticles,^{20–35} and were also utilized for analysis of SO_x distributions on catalytic nanoparticles.^{7,36} In particular, infrared nanospectroscopy measurements^{37,38} have shown that the types and adsorption geometries of SO_x species vary significantly due to morphological and structural heterogeneity among individual



nanoparticles.^{7,36} Using a similar approach, we have mapped the distribution and adsorption strength of surface ligands on Au nanocrystals with well-defined facets.³⁹

[View Article Online](#)
DOI: 10.1039/D5FD00139K

In this work, we employ atomic force microscopy infrared (AFM-IR) measurements to map the distribution of SO_x species on Pt nanocrystals (NCs) with well-defined facets. We find that the majority of SO_x species is adsorbed at a bidentate adsorption mode and reside on the more open facets and at inter-facet regions, whereas only a minority of SO_x occupy the flat (111) facets. Annealing to 200 °C led to desorption from edge sites, accompanied by transition from bidentate into tridentate adsorption mode. Further annealing to 300 °C led to desorption of most of the SO_x species, leaving residues near the center part of the nanocrystals, in which the SO_x is strongly adsorbed in a bidentate mode.

Experimental

Pt NCs preparation: 15 nm thick Pt film was e-beam evaporated on a sapphire crystal (c-plane oriented, Gavish) with a glove box evaporator (VST). Quartz crystal microbalance (QCM) measurements were used to assess the thickness of the evaporated film. NC were prepared by annealing the Pt-coated sapphire to 1000 °C for 2 minutes under N_2 atmosphere. The sample was then immersed in 10 Mm solution of H_2SO_4 for 1 h at room temperature. Afterward, the sample was transferred to a vial on a hot plate pre-heated to 100 °C for 10 minutes in air in order to remove physiosorbed residues. Annealing of the sample was performed under a nitrogen (N_2) atmosphere for 2 hours at the designated temperature.

Nano-IR measurements: AFM-IR measurements were performed at tapping mode using a nanoIR-3 (Bruker) setup equipped with a Bruker Hyperspectral QCL laser source (790-1950 cm^{-1}), gold-coated Si probes with a nominal diameter of ~25 nm, resonance frequencies of 75 ± 15 kHz, and spring constants of 1-7 N m^{-1} . Averaged spectral acquisition time was 5 seconds per spectrum with a spectral resolution of 2 cm^{-1} . The acquisition time was limited to 5 seconds to precisely define the measurement location and to prevent uncertainties caused by thermal drift.

Focused-ion beam (FIB): Dual Beam FIB instrument (FEI Helios) was employed for lamella extraction and the resulting lamella was analyzed by high-resolution scanning-transmission electron microscopy (STEM) operated at 300 kV.

X-ray photoelectron spectroscopy (XPS) measurements: Measurements were performed using Kratos AXIS Supra spectrometer (Kratos Analytical) with Al K α monochromatic X-ray source (1486.6 eV). XPS spectra were acquired with a takeoff angle of 90° (normal to analyzer), pass energy of 20 eV and step size of 0.1 eV; vacuum condition in the chamber was $2 \cdot 10^{-9}$ Torr. The binding energies were calibrated according to the C1s XPS peak position.

Results and discussion

To identify the sensitivity of different atomic facets in Pt particles to sulfur poisoning, we focused our study on analyzing the adsorption and desorption of SO_x species on Pt nanocrystals (NCs) with well-defined Wulff-like structures. The NCs were prepared by annealing and then exposed to H₂SO₄ to induce surface poisoning (see experimental section for details), following recently published procedures.^{7,36}

AFM topography images reveal NCs with lateral dimensions of 200-400 nm and height of up to 100 nm (Figure 1a). Exposure to H₂SO₄ did not lead to noticeable morphological changes. Two main NC morphologies were observed: elongated, hexagon-like NCs with distinctly longer opposing sides, yielding a more rectangular appearance (highlighted with a yellow circle in Figure 1a), and equilateral-like NCs resembling a rhombic structure (highlighted with a red circle in Figure 1a).⁴⁰

To identify the crystallographic facets of the NCs, a lamella was extracted from the sample using focused ion beam (FIB) milling, and transmission electron microscopy (TEM) images of both the hexagonal- and rhombic-like NCs were acquired (Figure 1c and 1d, respectively), along with their corresponding electron diffraction patterns (inset, Figure 1c and 1d). The hexagonal Pt nanocrystal exhibited a dominant (111) plane with adjacent (110) facets (Figure 1c). The smaller rhombic NC displayed multiple crystallographic orientations, including prominent (111), (001), and (113) planes (Figure 1d). The formation of these two distinct NC types is attributed to variations in local growth rates along different crystallographic directions, likely driven by subtle differences in the local defect density that influence facet stability. It is expected that these structural changes will impact the adsorption pattern of SO_x.⁴¹⁻⁴⁶



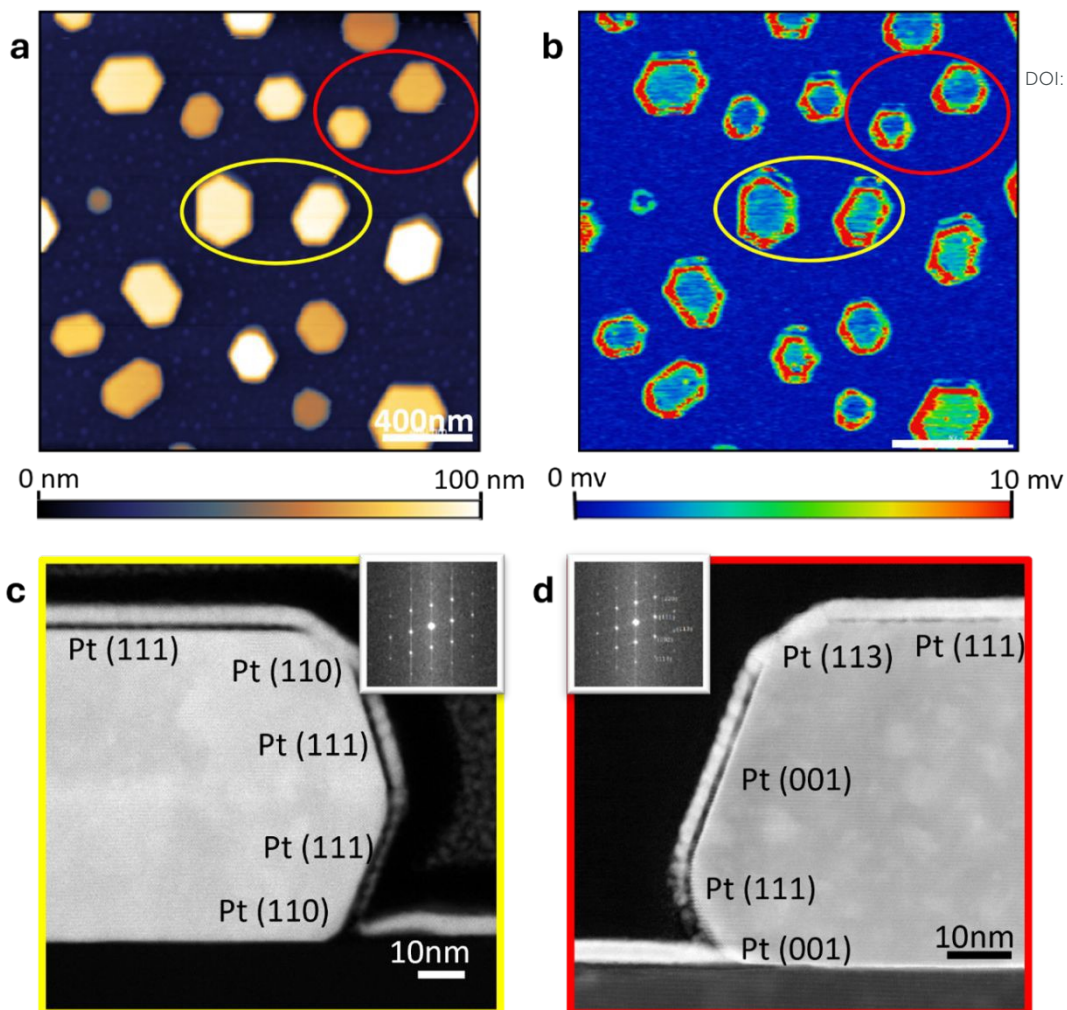


Figure 1. Characterization of Pt NCs. (a) AFM topography image of Pt NCs following sulfur poisoning. Representative hexagon- and rhombic-like NCs are circled in yellow and red, respectively. (b) AFM-IR map at 1100 cm^{-1} , that was acquired on the same area that was imaged by AFM. HR-TEM imaging of a cross section of hexagon NC (c) and rhombic NC (d), with their corresponding diffraction pattern (inset).

AFM-IR mapping was performed at 1100 cm^{-1} (Figure 1b), corresponds to the S-O vibration of sulfate anion,⁴⁷ on the same area imaged by AFM (Figure 1a). The IR signal intensity varied across the NCs, with higher signals detected at edges, steps, and the more open facets, while weaker signals appeared on the inner, flat (111) facets. These variations provide evidence for facet-dependent adsorption behavior and show the dominant role of nanocrystal structure in governing the local surface density of SO_x species.

Single NC analyses, including localized IR spectral measurements and AFM-IR mapping, were conducted to obtain high-resolution, sub-particle information on SO_x adsorption, distribution, and desorption (Figure 2). An AFM topography image of a hexagon-like NC is shown in Figure

2a(i). IR spectra were acquired at the edge and the center of the NC (measurement positions are indicated by red and black colored dots in Figure 2a(i)), and are presented in red and black colored spectra, respectively, in Figure 2a(ii). The spectra exhibit a broad feature spanning at

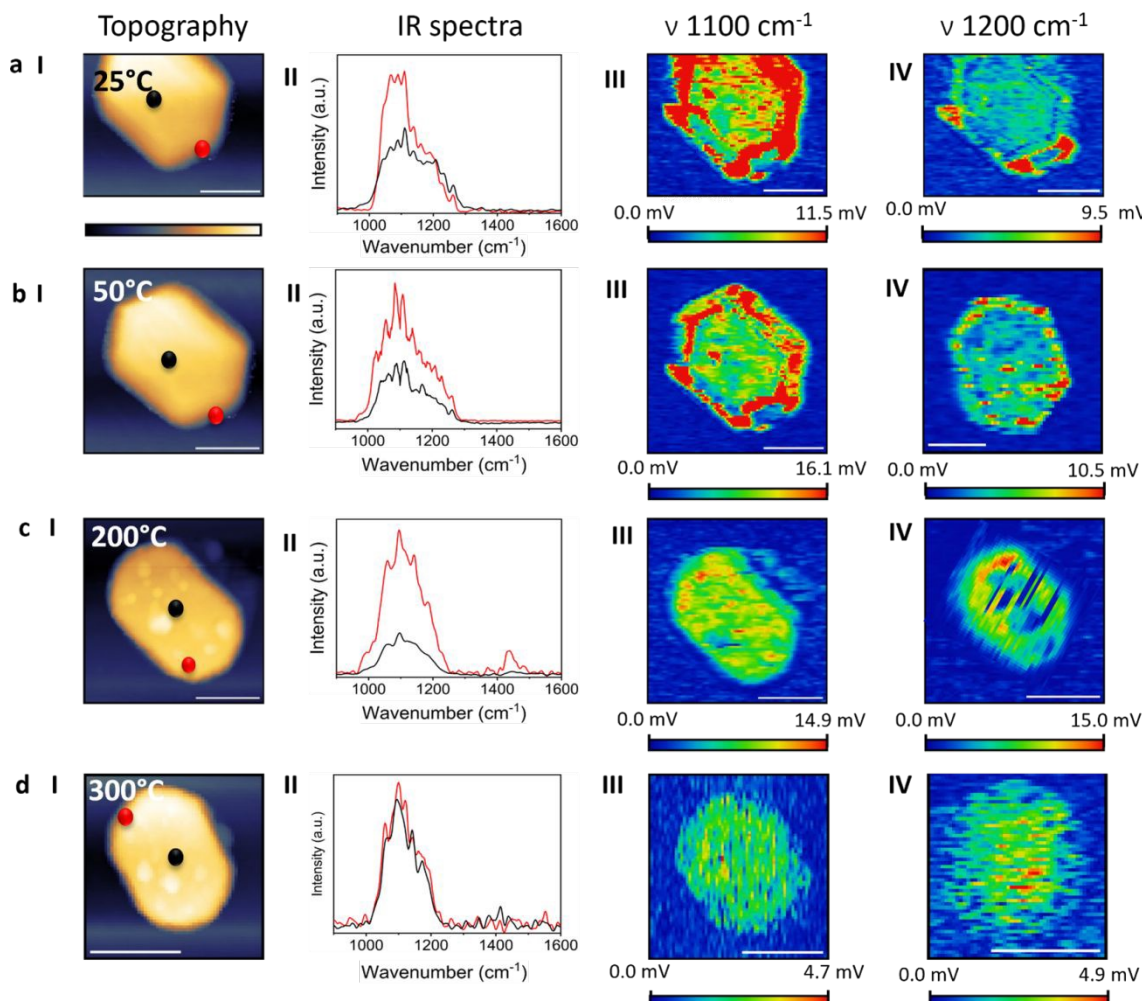


Figure 2. AFM-IR analysis of hexagon NC. AFM topography (i), localized IR spectra (ii) and AFM-IR mapping at 1100 cm^{-1} (iii) and 1200 cm^{-1} (iv), following surface poisoning by H_2SO_4 . Measurements were conducted at room temperature (a(i)-a(iv)), after annealing to $50\text{ }^\circ\text{C}$ (b(i)-b(iv)), $200\text{ }^\circ\text{C}$ (c(i)-c(iv)) and $300\text{ }^\circ\text{C}$ (d(i)-d(iv)). AFM topography images are shown in a(i), b(i), c(i) and d(i). IR spectra were acquired from the center (black-colored spectrum) and edge (red-colored spectrum) of a Pt NC and are shown in a(ii), b(ii), c(ii) and d(ii). The locations in which the IR measurements were acquired are indicated by black and red circles in the AFM topography images. The ratio between the red- and black-colored spectra reflects differences in signal intensities at different surface sites. Spectra shown in the different panels were normalized according to the amplitude of the red-colored spectra. The AFM images following annealing were acquired in different areas of the sample, and therefore different NCs were analyzed following each thermal treatment. Scale bar represents 200 nm.



1000-1280 cm^{-1} . The spectrum acquired at the center of the NC shows a stronger contribution in the 1000-1100 cm^{-1} region.

[View Article Online](#)
DOI: 10.1039/D5FD00139K

Sulfuric acid adsorbs on Pt primarily through bidentate and tridentate binding modes.^{7,48,49} The bidentate (2-fold) adsorption mode is energetically favored at undercoordinated sites such as edges, steps, and defects.^{44,50-53} Tridentate (3-fold) adsorption occurs when the sulfate species coordinates with three adjacent Pt atoms, a geometry which is mostly realized on atomically flat, close-packed terraces.^{7,11,36} It was demonstrated that sulfate is adsorbed on Pt(100) and Pt(110) with 2-fold geometry (C_{2v} symmetry) and induce two IR bands around 1100 and 1200 cm^{-1} , assigned to the stretching vibration of S-O bond in SO_4^{2-} coordinated to Pt atoms and that of the uncoordinated S-O bond, respectively. Sulfate adsorption on Pt(111) gives a single IR band at around 1200 cm^{-1} , which is assigned to the S-O stretching vibration of a 3-fold adsorption geometry.⁴⁷

The spectrum measured at the edge of the NC showed a higher signal at $\sim 1100 \text{ cm}^{-1}$, correlated to a dominant presence of sulfuric acid with a bidentate adsorption geometry on this site (red colored spectrum, Figure 2a(ii)). The IR signal that was acquired at the center of the NC showed a similar amplitude at the 1000-1250 cm^{-1} range, indicative that both bidentate and tridentate binding modes of sulfuric acid coexist on these sites (black colored spectrum, Figure 2a(ii)).

AFM-IR maps were acquired at 1100 and 1200 cm^{-1} (Figures 2a(iii) and 2a(iv), respectively) to identify the spatial distribution of bidentate and tridentate adsorption modes across the facets of the NCs. The IR map at 1100 cm^{-1} (Figure 2a(iii)) shows strong signal intensities at the nanocrystal edges and on the side Pt(110) facets, with reduced intensity at the NC center. AFM-IR mapping at 1200 cm^{-1} (Figure 2a(iv)) exhibits weaker signals, that were primarily localized at inter-facet regions and edge sites. The IR mapping support the results obtained in the localized IR spectra and show that there is a preference toward a 2-fold adsorption geometry at sites with low-coordinated surface atoms.

Integration of the IR mapping and spectroscopy data reveals that the surface structure of Pt NCs governs the surface distribution of SO_x . The spectral signature associated with the 2-fold (bidentate) adsorption mode of sulfate ($\sim 1100 \text{ cm}^{-1}$) was detected across most regions of the NCs, with high signal variability across the NC. Higher signal intensity was observed on the side facets and at inter-facet regions, whereas lower intensity appeared on the flat Pt(111) terraces. The spectral signature corresponding to the 3-fold (tridentate) adsorption mode



($\sim 1200 \text{ cm}^{-1}$) was weaker, and was characterized with local enhancement at inter-facet and the more open (110) facets.

[View Article Online](#)
DOI: 10.1039/D5FD00139K

To obtain a quantitative measure of the spatial distribution of SO_x species, the NC was segmented into concentric rings at increasing radial distances from its center. The IR signal amplitude within each ring was averaged and the averaged IR intensities, analyzed from the IR maps at 1100 and 1200 cm^{-1} , were plotted as a function of the radial distance of each concentric ring from the NC center (Figures 3a and 3b, respectively). This analysis revealed a detectable spectral contribution at the NC center for the IR signal at 1100 cm^{-1} (black-colored curve, Figure 3a) and a pronounced $\sim 50\%$ enhancement in the IR intensity at a radial distance of approximately 75 nm , corresponding to inter-facet regions where SO_x species preferentially accumulate. Quantitative analysis of the IR mapping at 1200 cm^{-1} (black-colored curve, Figure 3b) showed a lower and much more homogeneous signal, with a relatively small increase at the particle's rim. These results show that the distribution of SO_x species at a tridentate binding mode is more consistent on the NC's surface, in comparison to the dominant bidentate mode that was mainly probed at inter-facets and side facets.

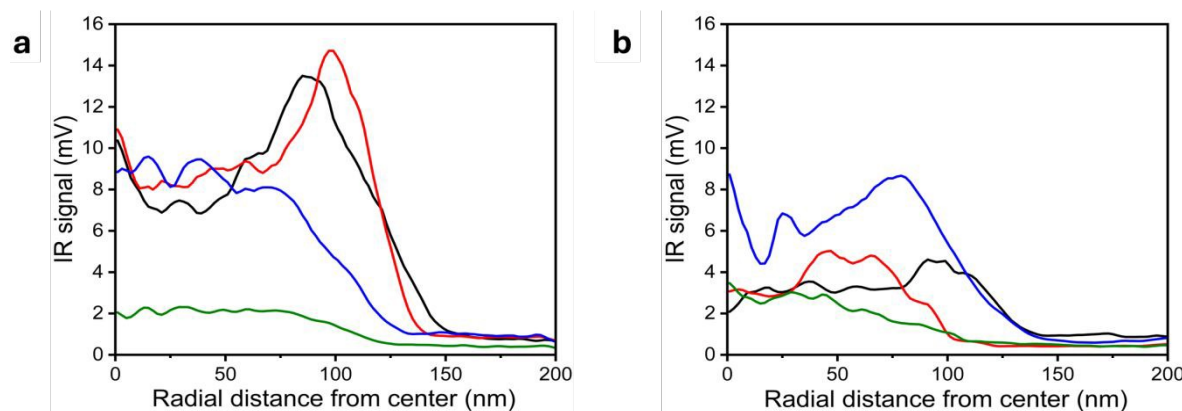


Figure 3. Quantitative analysis of AFM-IR maps. The AFM-IR maps shown in Figure 2 were analyzed by dividing each nanocrystal into concentric rings originating from its center. The AFM-IR signal within each ring was extracted and averaged to obtain the mean intensities at 1100 cm^{-1} (a) and 1200 cm^{-1} (b) as a function of the radial distance of the ring from the nanocrystal center. This analysis was performed for IR maps that were acquired at room temperature (black-colored curves), after annealing to $50 \text{ }^\circ\text{C}$ (red-colored curves), $200 \text{ }^\circ\text{C}$ (blue-colored curves) and $300 \text{ }^\circ\text{C}$ (green-colored curves).

Analysis of the IR signal at room temperature reveals a clear preference for SO_x adsorption at bidentate adsorption mode on edge sites and on more open facets. The bidentate mode was consistently more prominent than the tridentate mode, and more heterogeneous in its dispersion

on the NC surface. This indicates competitive adsorption at identical surface sites, with the energetically less demanding bidentate configuration dominating under ambient conditions. [View Article Online](#) [FD00139K](#)

IR maps and localized IR spectra were acquired following annealing to 50 °C (Figure 2b). The localized IR spectra showed lower intensity in the high-wavenumber contribution, resulting in a more pronounced peak near 1100 cm⁻¹ (Figure 2b(ii)). The IR map at 1100 cm⁻¹ (Figure 2b(iii)) showed a decrease in the overall signal intensity and a stronger localization at inter-facet regions. Averaged analysis of the IR signal revealed enhanced localization of the 1100 cm⁻¹ signal at inter-facet regions (Figure 3a, red-colored curve). The IR map at 1200 cm⁻¹ (Figure 2b(iv)) exhibited a more spatially dispersed signal after annealing, with some preference to inter-facet sites, as also identified in the quantitative analysis (Figure 3b, red-colored curve). These results indicate that mild annealing promotes localization of bidentate species on inter-facet sites, which contain higher densities of surface defects, whereas tridentate species diffuse inward toward flatter regions, that facilitates the 3-fold binding geometry.

This trend was enhanced following annealing to 200 °C (Figure 2c). After annealing, the IR spectrum exhibited a dominant peak at 1100 cm⁻¹ with a substantially diminished 1200 cm⁻¹ contribution (Figure 2c(ii)). The peak at 1420 cm⁻¹, which was detected in the IR spectra acquired at edge sites, is attributed to carboxylate species that was formed on the NC surface following exposure of organic residues to high temperature. IR mapping at 1100 cm⁻¹ showed a lower signal intensity at inter-facet sites, and the signal amplitude at the NC center became comparable to the one measured at the edges, as also indicated in the quantitative analysis (Figure 3a, blue-colored curve). In contrast, AFM-IR mapping at 1200 cm⁻¹ showed an overall increase in signal intensity and specifically at edge sites (Figure 2c(iv)), consistent with the averaged IR analysis (Figure 3b, blue-colored curve). These findings suggest that annealing to 200 °C promotes a transition from bidentate to tridentate adsorption mode, enabled by the added thermal energy required to activate this transition.

Further annealing to 300 °C led to sharpening and localization of the IR peak to the 1020-1220 cm⁻¹ region at both the center and the edge of the NC (Figure 2d(ii)), and the spectral amplitudes at these locations became comparable, indicative of desorption from edge sites. IR mapping at 1100 cm⁻¹ (Figure 2d(iii)) showed a pronounced decrease in signal intensity across the NC (Figure 3a, green-colored curve), with the averaged value in the interior region lower by ~80% compared to the signal measured at room temperature.

IR mapping at 1200 cm^{-1} showed a reduced signal at the outer regions of the NC, yet significant intensity persisted at the NC interior even after annealing to $300\text{ }^\circ\text{C}$ (Figure 2d(iv) and Figure 3b, green-colored curve). These results indicate that after annealing to $300\text{ }^\circ\text{C}$, SO_x species are no longer detected at inter-facet sites, whereas tridentate is the favored configurations on the interior part of the NC. This highlights the higher thermal stability of SO_x species bound at a tridentate mode to flat, highly coordinated regions compared to the more reactive edge sites.

A similar temperature-dependent analysis was conducted for a more symmetric NC (Figure 4a(i)). IR spectra were acquired at the edge and center of the NC and displayed a broad IR band spanning $1000\text{-}1300\text{ cm}^{-1}$, with a stronger signal at the edge of the NC (Figure 4a(ii)). IR mapping at 1100 cm^{-1} revealed a pronounced signal on side facets and inter-facet regions (Figure 4a(iii)), whereas the 1200 cm^{-1} feature appeared weaker and spatially confined (Figure 4a(iv)). In both cases, the IR intensity was highest on the side facets and lower on the flat (111) facet, consistent with the quantitative IR mapping analysis (Figure 5, black-colored curves). The dominant signal at 1100 cm^{-1} indicates the preference toward a bidentate adsorption geometry, which is further enhanced on side facets.

Annealing to $50\text{ }^\circ\text{C}$ led to a lower amplitude in the $1200\text{-}1300\text{ cm}^{-1}$ range for the spectra measured at the side of the NC (red-colored spectrum, Figure 4b(ii)), while sharper and more distinct contributions in the $1200\text{-}1300\text{ cm}^{-1}$ region were probed in the spectra measured at the center of the NC (black-colored spectrum, Figure 4b(ii)). Correspondingly, the IR maps showed lower overall signal intensities and more localized features (Figure 4b(iii)–(iv)), consistent with desorption from edge sites, as also validated by the quantitative IR analysis (Figure 5, red-colored curves).

Further annealing to $200\text{ }^\circ\text{C}$ resulted in an additional decrease in the $1200\text{-}1300\text{ cm}^{-1}$ range (Figure 4c(ii)). The improved signal-to-noise ratio observed in the black-colored spectrum in panel c(ii) is attributed to a local increase in the surface density of the adsorbed species, which also results in a relatively higher signal compared to other spectra that were acquired at the center of the NCs. The IR map at 1100 cm^{-1} showed a substantial reduction in signal intensity across the NC (Figure 4c(iii)), and the quantitative analysis (Figure 5a, blue-colored curve) confirmed a major overall decrease. IR map at 1200 cm^{-1} revealed a lower overall signal amplitude (Figure 4c(iv)), verified by quantitative analysis (Figure 5b, blue-colored curve). Thus, annealing to $200\text{ }^\circ\text{C}$ promoted desorption, and specifically desorption from edge sites.



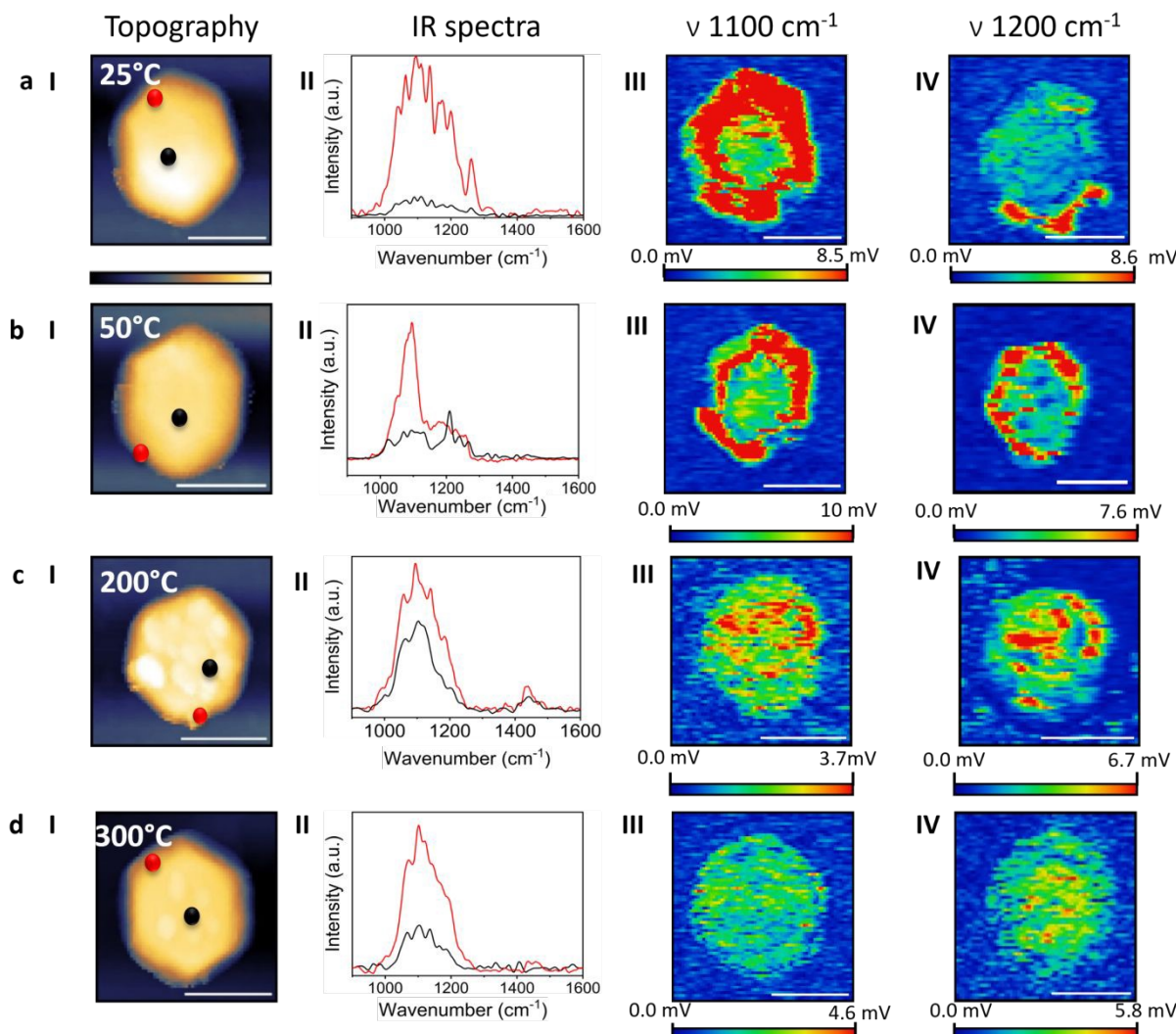


Figure 4. AFM-IR mapping of a single NC. AFM topography (i), localized IR spectra (ii) and AFM-IR mapping at 1100 cm^{-1} (iii) and 1200 cm^{-1} (iv), following surface poisoning by H_2SO_4 . Measurements were conducted at room temperature (a(i)-a(iv)), after annealing to $50\text{ }^\circ\text{C}$ (b(i)-b(iv)), $200\text{ }^\circ\text{C}$ (c(i)-c(iv)) and $300\text{ }^\circ\text{C}$ (d(i)-d(iv)). AFM topography images are shown in a(i), b(i), c(i) and d(i). IR spectra were acquired from the center (black-colored spectrum) and edge (red-colored spectrum) of a Pt NC and are shown in a(ii), b(ii), c(ii) and d(ii). The locations in which the IR measurements were acquired are indicated by black and red circles in the AFM topography images. The ratio between the red- and black-colored spectra reflects differences in signal intensities at different surface sites. All spectra shown in the different panels were normalized according to the amplitude of the red-colored spectra. The AFM images following annealing were acquired in different areas of the sample, and therefore different NCs were analyzed following each thermal treatment. Scale bar represents 200 nm.

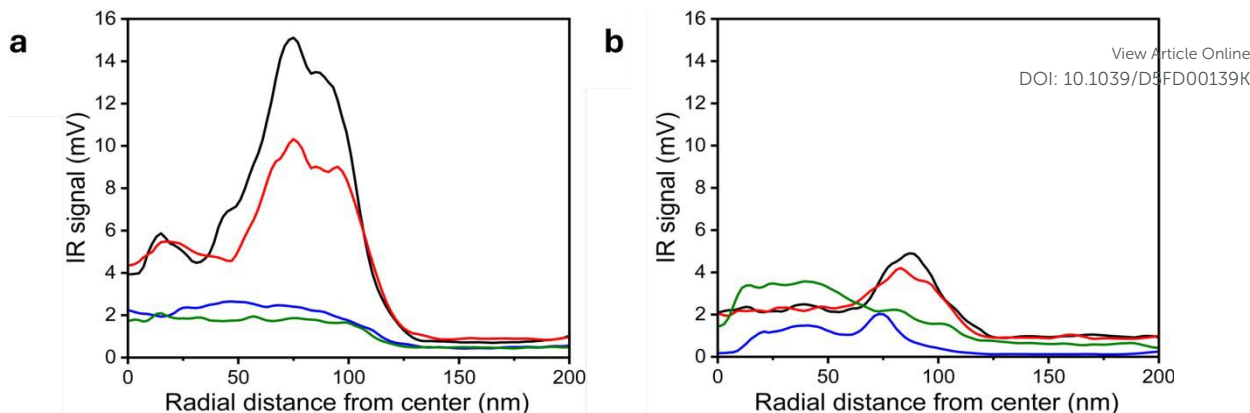


Figure 5. Quantitative analysis of AFM-IR. The AFM-IR maps shown in Figure 4 were analyzed by dividing each nanocrystal into concentric rings originating from its center. The AFM-IR signal within each ring was extracted and averaged to obtain the mean intensities at 1100 cm^{-1} (a) and 1200 cm^{-1} (b) as a function of the radial distance of the ring from the nanocrystal center. This analysis was performed for IR maps that were acquired at room temperature (black-colored curves), after annealing to $50\text{ }^{\circ}\text{C}$ (red-colored curves), $200\text{ }^{\circ}\text{C}$ (blue-colored curves) and $300\text{ }^{\circ}\text{C}$ (green-colored curves).

Local IR spectra were measured after annealing to $300\text{ }^{\circ}\text{C}$ and showed a stronger signal at the edges of the NC (Figure 4d(ii)). IR maps (Figure 4d(iii) and (iv)) and their quantitative analysis (Figure 5a, green-colored curve) revealed that annealing to $300\text{ }^{\circ}\text{C}$ led to a minor decrease in the averaged 1100 cm^{-1} intensity. The 1200 cm^{-1} signal at the center of the NC increased following annealing (Figure 5b, green-colored curve), indicating a diffusion of the tridentate species to the central region of the NC and transformation from bidentate to the tridentate adsorption mode.

Integration of the nanoscale measurements demonstrates clear temperature-dependent changes in both the surface density and adsorption mode of SO_x species. At room temperature, SO_x adsorption is nonuniform, with higher coverage at defect-rich inter-facet and side-facet regions, and a preference for the bidentate adsorption mode. Annealing to $200\text{ }^{\circ}\text{C}$ results in selective desorption from edge sites and a shift from bidentate to tridentate adsorption at the NC interior. This trend becomes more pronounced after annealing to $300\text{ }^{\circ}\text{C}$, where SO_x species persist primarily at the NC center and show preference toward the tridentate adsorption mode.

Temperature-dependent S2p X-ray photoelectron spectra (XPS) were acquired to complement the nanospectroscopy analysis (Figure 6). At room-temperature the XP spectrum (red-colored spectrum, Figure 6), showed a strong peak at 169.0 eV , characteristic of S^{6+} in sulfate species, along with contributions from S^{4+} in SO_2 related species. Following annealing to $50\text{ }^{\circ}\text{C}$ (blue-



colored spectrum, Figure 6), the 169.0 eV peak showed a decrease in intensity, consistent with partial desorption, along with a broader peak profile, indicating the coexistence of various SO_x species adsorbed in different adsorption geometries.

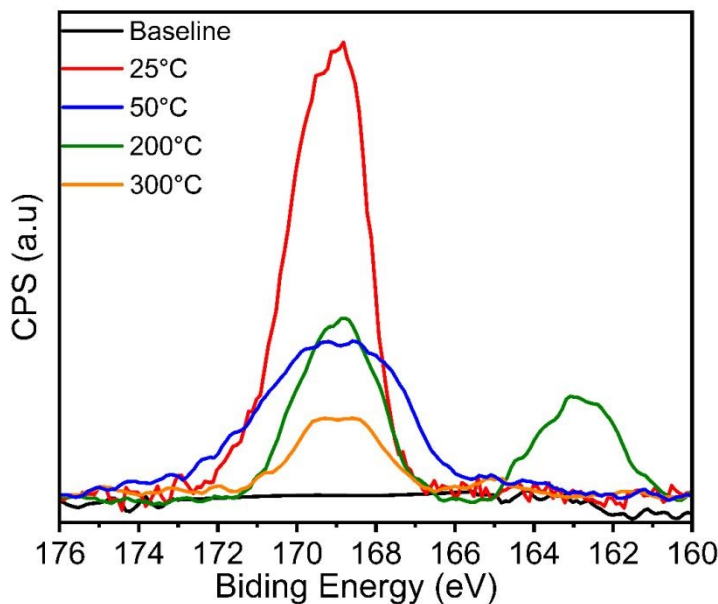


Figure 6. S2p XP spectra of Pt NCs before (black-colored spectrum) and after their exposure to H_2SO_4 . XPS measurements of the poisoned NCs were acquired at room temperature (red-colored spectrum) and after annealing to 50 °C (blue-colored spectrum), 200 °C (green-colored spectrum) and 300 °C (orange-colored spectrum).

Following annealing to 200 °C (green-colored spectrum, Figure 6), the peak centered at 169.0 eV was narrowed and a new signal was detected at 163.0 eV, correlated to sulfur at lower oxidation states (S^0 , S^{1-} , or S^{2-}). This likely follows a sequence of surface mediated reduction steps, consistent with previous studies,^{54–56} and marks the onset of thermal reduction, followed by desorption. Further annealing to 300 °C (orange-colored spectrum, Figure 6) leads to a substantial decrease in signal amplitude. This result highlights the thermal desorption of SO_x species from the surface of Pt NCs at relatively moderate temperatures.^{57,58} The fact that these transformations occur under N_2 environment further confirms that Pt NCs catalyze the selective reduction and removal of surface bound SO_x through thermal activation, which is facilitated on sites that are characterized with high density of surface defects.

Conclusions

AFM-IR nanospectroscopy measurements reveals that sulfate adsorption on Pt NCs is strongly governed by local coordination and facet structure. Defect-rich edges, steps, and inter-facet



regions serve as high-affinity sites that predominantly stabilize bidentate sulfate, whereas flat Pt(111)-like terraces exhibit lower overall coverage and a stronger tendency toward tridentate coordination. Temperature-dependent measurements show that annealing triggers selective desorption from undercoordinated sites and promotes diffusion of sulfate species into terrace regions, where the transition from bidentate to tridentate adsorption becomes thermodynamically favored. Upon annealing to 300 °C, most SO_x species detach from edge sites, leaving behind a small population of thermally persistent tridentate species bound to terrace atoms. These findings, which were supported by XPS measurements, establish a direct correlation between facet geometry, adsorption mode, and thermal stability of SO_x species, offering fundamental insights into site-dependent poisoning and regeneration processes in Pt-based catalysts.

Data availability

Data for this article are available at Zenodo at 10.5281/zenodo.17778202.

Author contributions

The manuscript was written through contributions of all authors. All authors have given approval to the final version of the manuscript. Conceptualization, methodology and data curation: LR and EG; formal analysis: YH and EG; writing – original draft: LR; writing – review & editing: EG; supervision: EG

Conflicts of interest

There are no conflicts to declare.

Acknowledgements

This research was supported by the Israel Science Foundation grant (Grant Agreement No. 2118/22). The authors acknowledge Dr. Sergei Remennik (Hebrew University Center for Nanoscience and Nanotechnology) for conducting HR-TEM and diffraction measurements.



References

View Article Online

DOI: 10.1039/D5FD00139K

(1) Argyle, M. D.; Bartholomew, C. H. Heterogeneous Catalyst Deactivation and Regeneration: A Review. *Catalysts*. **2015**, pp 145–269. <https://doi.org/10.3390/catal5010145>.

(2) Hare, B. J.; Garcia Carcamo, R. A.; Daemen, L. L.; Cheng, Y.; Getman, R. B.; Sievers, C. Poisoning of Pt/ γ -Al₂O₃ Aqueous Phase Reforming Catalysts by Ketone and Diketone-Derived Surface Species. *ACS Catal* **2024**, *14* (3), 1480–1493. <https://doi.org/10.1021/acscatal.3c04774>.

(3) Chen, W.; Cao, J.; Fu, W.; Zhang, J.; Qian, G.; Yang, J.; Chen, D.; Zhou, X.; Yuan, W.; Duan, X. Molecular-Level Insights into the Notorious CO Poisoning of Platinum Catalyst. *Angewandte Chemie - International Edition* **2022**, *61* (16). <https://doi.org/10.1002/anie.202200190>.

(4) Kim, K. J.; Lee, Y. L.; Hong, G. R.; Ahn, S. Y.; Kim, B. J.; Lee, S. S.; Jeon, Y.; Roh, H. S. A Study on the Activity Recovery Behavior of Noble Metal Catalysts against Sulfur Poisoning. *Catal Today* **2024**, *425*. <https://doi.org/10.1016/j.cattod.2023.114361>.

(5) Liu, S.; Wang, T.; Wu, X.; Li, J.; Liu, S.; Ran, R. Sulfur Poisoning and Thermal Regeneration of Silica-Alumina Supported Platinum Catalyst for Soot Oxidation. *Surfaces and Interfaces* **2025**, *68*. <https://doi.org/10.1016/j.surfin.2025.106732>.

(6) Awad, M. I.; Saleh, M. M.; Ohsaka, T. Impact of SO₂ Poisoning of Platinum Nanoparticles Modified Glassy Carbon Electrode on Oxygen Reduction. *J Power Sources* **2011**, *196* (8), 3722–3728. <https://doi.org/10.1016/j.jpowsour.2010.12.080>.

(7) Say, Z.; Kaya, M.; Kaderoglu, C.; Koçak, Y.; Ercan, K. E.; Sika-Nartey, A. T.; Jalal, A.; Turk, A. A.; Langhammer, C.; Jahangirzadeh Varjovi, M.; Durgun, E.; Ozensoy, E. Unraveling Molecular Fingerprints of Catalytic Sulfur Poisoning at the Nanometer Scale with Near-Field Infrared Spectroscopy. *J Am Chem Soc* **2022**, *144* (19), 8848–8860. <https://doi.org/10.1021/jacs.2c03088>.

(8) Wilburn, M. S.; Epling, W. S. Formation and Decomposition of Sulfite and Sulfate Species on Pt/Pd Catalysts: An SO₂ Oxidation and Sulfur Exposure Study. *ACS Catal* **2019**, *9* (1), 640–648. <https://doi.org/10.1021/acscatal.8b03529>.

(9) Gaudin, L. F.; Kang, M.; Bentley, C. L. Facet-Dependent Electrocatalysis and Surface Electrochemical Processes on Polycrystalline Platinum. *Electrochim Acta* **2023**, *450*. <https://doi.org/10.1016/j.electacta.2023.142223>.

(10) Ungerer, M. J.; Van Sittert, C. G. C. E.; De Leeuw, N. H. Behavior of S, SO, and SO₃ on Pt (001), (011), and (111) Surfaces: A DFT Study. *Journal of Chemical Physics* **2021**, *154* (19). <https://doi.org/10.1063/5.0043501>.

(11) Hoshi, N.; Sakurada, A.; Nakamura, S.; Teruya, S.; Koga, O.; Hori, Y. Infrared Reflection Absorption Spectroscopy of Sulfuric Acid Anion Adsorbed on Stepped Surfaces of Platinum Single-Crystal Electrodes. *Journal of Physical Chemistry B* **2002**, *106* (8), 1985–1990. <https://doi.org/10.1021/jp012456o>.

(12) Mostany, J.; Herrero, E.; Feliu, J. M.; Lipkowski, J. Thermodynamic Studies of Anion Adsorption at Stepped Platinum(Hkl) Electrode Surfaces in Sulfuric Acid Solutions. *Journal of Physical Chemistry B* **2002**, *106* (49), 12787–12796. <https://doi.org/10.1021/jp026561p>.

(13) Aoki, M.; Shishido, T.; Morooka, T.; Nakanishi, T.; Masuda, T. Electrochemical Oxidative Desorption of Adsorbed Sulfur Species on (111) Surfaces of Single Crystals of Pure Pt and Pt-Based Bimetallic Alloys. *Journal of Physical Chemistry C* **2025**, *129* (4), 2122–2131. Article Online DOI: 10.1039/D5FD00139K <https://doi.org/10.1021/acs.jpcc.4c06652>.

(14) Hossain, M. J.; Rahman, M. M.; Jafar Sharif, M. Preference for Low-Coordination Sites by Adsorbed CO on Small Platinum Nanoparticles. *Nanoscale Adv* **2020**, *2* (3), 1245–1252. <https://doi.org/10.1039/c9na00499h>.

(15) Rhee, C. K.; Kim, B. J.; Ham, C.; Kim, Y. J.; Song, K.; Kwon, K. Size Effect of Pt Nanoparticle on Catalytic Activity in Oxidation of Methanol and Formic Acid: Comparison to Pt(111), Pt(100), and Polycrystalline Pt Electrodes. *Langmuir* **2009**, *25* (12), 7140–7147. <https://doi.org/10.1021/la900204c>.

(16) Van Loon, J.; Kubarev, A. V.; Roeffaers, M. B. J. Correlating Catalyst Structure and Activity at the Nanoscale. *ChemNanoMat* **2018**, pp 6–14. <https://doi.org/10.1002/cnma.201700301>.

(17) Groot, I. M. N. Investigation of Active Catalysts at Work. *Acc Chem Res* **2021**, *54* (23), 4334–4341. <https://doi.org/10.1021/acs.accounts.1c00429>.

(18) Choi, J. I. J.; Kim, T. S.; Kim, D.; Lee, S. W.; Park, J. Y. Operando Surface Characterization on Catalytic and Energy Materials from Single Crystals to Nanoparticles. *ACS Nano*. American Chemical Society **2020**, pp 16392–16413. <https://doi.org/10.1021/acsnano.0c07549>.

(19) Xu, W.; Kong, J. S.; Yeh, Y. T. E.; Chen, P. Single-Molecule Nanocatalysis Reveals Heterogeneous Reaction Pathways and Catalyticdynamics. *Nat Mater* **2008**, *7* (12), 992–996. <https://doi.org/10.1038/nmat2319>.

(20) Roeffaers, M. B. J.; De Cremer, G.; Libeert, J.; Ameloot, R.; Dedecker, P.; Bons, A. J.; Bückins, M.; Martens, J. A.; Sels, B. F.; De Vos, D. E.; Hofkens, J. Super-Resolution Reactivity Mapping of Nanostructured Catalyst Particles. *Angewandte Chemie - International Edition* **2009**, *48* (49), 9285–9289. <https://doi.org/10.1002/anie.200904944>.

(21) Dery, S.; Friedman, B.; Shema, H.; Gross, E. Mechanistic Insights Gained by High Spatial Resolution Reactivity Mapping of Homogeneous and Heterogeneous (Electro)Catalysts. *Chemical Reviews*. American Chemical Society **2023**, pp 6003–6038. <https://doi.org/10.1021/acs.chemrev.2c00867>.

(22) Rikanati, L.; Dery, S.; Gross, E. AFM-IR and s-SNOM-IR Measurements of Chemically Addressable Monolayers on Au Nanoparticles. *Journal of Chemical Physics* **2021**, *155* (20). <https://doi.org/10.1063/5.0072079>.

(23) Mao, X.; Liu, C.; Hesari, M.; Zou, N.; Chen, P. Super-Resolution Imaging of Non-Fluorescent Reactions via Competition. *Nat Chem* **2019**, *11* (8), 687–694. <https://doi.org/10.1038/s41557-019-0288-8>.

(24) Wu, C. Y.; Wolf, W. J.; Levartovsky, Y.; Bechtel, H. A.; Martin, M. C.; Toste, F. D.; Gross, E. High-Spatial-Resolution Mapping of Catalytic Reactions on Single Particles. *Nature* **2017**, *541* (7638), 511–515. <https://doi.org/10.1038/nature20795>.

(25) Dery, S.; Mehlman, H.; Hale, L.; Carmiel-Kostan, M.; Yemini, R.; Ben-Tzvi, T.; Noked, M.; Toste, F. D.; Gross, E. Site-Independent Hydrogenation Reactions on Oxide-Supported Au



Nanoparticles Facilitated by Intraparticle Hydrogen Atom Diffusion. *ACS Catal* **2021**, *11* (15), 9875–9884. <https://doi.org/10.1021/acscatal.1c01987>.

[View Article Online](#)

DOI: 10.1039/D5FD00139K

(26) Li, Z.; Kurouski, D. Plasmon-Driven Chemistry on Mono- And Bimetallic Nanostructures. *Acc Chem Res* **2021**, *54* (10), 2477–2487. <https://doi.org/10.1021/acs.accounts.1c00093>.

(27) Friedman, B.; Giloni, L.; Gazit, O. M.; Gross, E. Nanoscale Chemical Imaging of Basic Sites Distribution on Catalytically Active Mg–Al Mixed Oxide Particles. *Chemical and Biomedical Imaging* **2025**, *3* (8), 560–568. <https://doi.org/10.1021/cbmi.5c00017>.

(28) Karreman, M. A.; Buurmans, I. L. C.; Geus, J. W.; Agronskaia, A. V.; Ruiz-Martínez, J.; Gerritsen, H. C.; Weckhuysen, B. M. Integrated Laser and Electron Microscopy Correlates Structure of Fluid Catalytic Cracking Particles to Brønsted Acidity. *Angewandte Chemie - International Edition* **2012**, *51* (6), 1428–1431. <https://doi.org/10.1002/anie.201106651>.

(29) Dery, S.; Kim, S.; Feferman, D.; Mehlman, H.; Toste, F. D.; Gross, E. Site-Dependent Selectivity in Oxidation Reactions on Single Pt Nanoparticles. *Physical Chemistry Chemical Physics* **2020**, *22* (34), 18765–18769. <https://doi.org/10.1039/d0cp00642d>.

(30) Dery, S.; Kim, S.; Haddad, D.; Cossaro, A.; Verdini, A.; Floreano, L.; Toste, F. D.; Gross, E. Identifying Site-Dependent Reactivity in Oxidation Reactions on Single Pt Particles. *Chem Sci* **2018**, *9* (31), 6523–6531. <https://doi.org/10.1039/c8sc01956h>.

(31) Ruiz-Martínez, J.; Beale, A. M.; Deka, U.; O'Brien, M. G.; Quinn, P. D.; Mosselmans, J. F. W.; Weckhuysen, B. M. Correlating Metal Poisoning with Zeolite Deactivation in an Individual Catalyst Particle by Chemical and Phase-Sensitive X-Ray Microscopy. *Angewandte Chemie - International Edition* **2013**, *52* (23), 5983–5987. <https://doi.org/10.1002/anie.201210030>.

(32) Kox, M. H. F.; Domke, K. F.; Day, J. P. R.; Rago, G.; Stavitski, E.; Bonn, M.; Weckhuysen, B. M. Label-Free Chemical Imaging of Catalytic Solids by Coherent Anti-Stokes Raman Scattering and Synchrotron-Based Infrared Microscopy. *Angewandte Chemie - International Edition* **2009**, *48* (47), 8990–8994. <https://doi.org/10.1002/anie.200904282>.

(33) Busch, O. M.; Brijoux, W.; Thomson, S.; Schüth, F. Spatially Resolving Infrared Spectroscopy for Parallelized Characterization of Acid Sites of Catalysts via Pyridine Sorption: Possibilities and Limitations. *J Catal* **2004**, *222* (1), 174–179. <https://doi.org/10.1016/j.jcat.2003.11.002>.

(34) De Cremer, G.; Bartholomeeusen, E.; Pescarmona, P. P.; Lin, K.; De Vos, D. E.; Hofkens, J.; Roeffaers, M. B. J.; Sels, B. F. The Influence of Diffusion Phenomena on Catalysis: A Study at the Single Particle Level Using Fluorescence Microscopy. In *Catalysis Today*; **2010**; Vol. 157, pp 236–242. <https://doi.org/10.1016/j.cattod.2010.04.035>.

(35) Bergwerff, J. A.; Visser, T.; Leliveld, B. R. G.; Rossenaar, B. D.; De Jong, K. P.; Weckhuysen, B. M. Envisaging the Physicochemical Processes during the Preparation of Supported Catalysts: Raman Microscopy on the Impregnation of Mo onto Al 2O3 Extrudates. *J Am Chem Soc* **2004**, *126* (44), 14548–14556. <https://doi.org/10.1021/ja040107c>.

(36) Kostan-Carmiel, M.; Theodoridis, A.; Eisenberg, H. R.; Stein, T.; Langhammer, C.; Gross, E. Nanoscale Analysis of Sulfur Poisoning Effects on Hydrogen Sorption in Single Pd Nanoparticles. *ACS Nano* **2025**, *19* (42), 36969–36981. <https://doi.org/10.1021/acsnano.5c08917>.



(37) Dazzi, A.; Prater, C. B. AFM-IR: Technology and Applications in Nanoscale Infrared Spectroscopy and Chemical Imaging. *Chemical Reviews. American Chemical Society* **2017**, pp 5146–5173. <https://doi.org/10.1021/acs.chemrev.6b00448>. Article Online DOI: 10.1039/D5FD00139K

(38) Kurouski, D.; Dazzi, A.; Zenobi, R.; Centrone, A. Infrared and Raman Chemical Imaging and Spectroscopy at the Nanoscale. *Chemical Society Reviews. Royal Society of Chemistry* **2020**, pp 3315–3347. <https://doi.org/10.1039/c8cs00916c>.

(39) Rikanati, L.; Shema, H.; Ben-Tzvi, T.; Gross, E. Nanoimaging of Facet-Dependent Adsorption, Diffusion, and Reactivity of Surface Ligands on Au Nanocrystals. *Nano Lett* **2023**, *23* (12), 5437–5444. <https://doi.org/10.1021/acs.nanolett.3c00250>.

(40) Zhang, B.; Wang, D.; Hou, Y.; Yang, S.; Yang, X. H.; Zhong, J. H.; Liu, J.; Wang, H. F.; Hu, P.; Zhao, H. J.; Yang, H. G. Facet-Dependent Catalytic Activity of Platinum Nanocrystals for Triiodide Reduction in Dye-Sensitized Solar Cells. *Sci Rep* **2013**, *3*. <https://doi.org/10.1038/srep01836>.

(41) Wongbua-ngam, P.; Veerasai, W.; Wilairat, P.; Kheowan, O. U. Model Interpretation of Electrochemical Behavior of Pt/H₂SO₄ Interface over Both the Hydrogen Oxidation and Oxide Formation Regions. *Int J Hydrogen Energy* **2019**, *44* (23), 12108–12117. <https://doi.org/10.1016/j.ijhydene.2019.03.076>.

(42) Huang, M. H.; Rej, S.; Hsu, S. C. Facet-Dependent Properties of Polyhedral Nanocrystals. *Chemical Communications* **2014**, *50* (14), 1634–1644. <https://doi.org/10.1039/c3cc48527g>.

(43) Han, B. C.; Miranda, C. R.; Ceder, G. Effect of Particle Size and Surface Structure on Adsorption of O and OH on Platinum Nanoparticles: A First-Principles Study. *Phys Rev B Condens Matter Mater Phys* **2008**, *77* (7). <https://doi.org/10.1103/PhysRevB.77.075410>.

(44) Hoshi, N.; Kuroda, M.; Ogawa, T.; Koga, O.; Hori, Y. Infrared Reflection Absorption Spectroscopy of the Sulfuric Acid Anion Adsorbed on Pd(S)-[n(111) × (111)] Electrodes. *Langmuir* **2004**, *20* (12), 5066–5070. <https://doi.org/10.1021/la036149g>.

(45) Zeng, X. M.; Huang, R.; Shao, G. F.; Wen, Y. H.; Sun, S. G. High-Index-Faceted Platinum Nanoparticles: Insights into Structural and Thermal Stabilities and Shape Evolution from Atomistic Simulations. *J Mater Chem A Mater* **2014**, *2* (29), 11480–11489. <https://doi.org/10.1039/c4ta01731e>.

(46) Mastronardi, V.; Magliocca, E.; Gullon, J. S.; Brescia, R.; Pompa, P. P.; Miller, T. S.; Moglianetti, M. Ultrasmall, Coating-Free, Pyramidal Platinum Nanoparticles for High Stability Fuel Cell Oxygen Reduction. *ACS Appl Mater Interfaces* **2022**, *14* (32), 36570–36581. <https://doi.org/10.1021/acsami.2c07738>.

(47) Hoshi, N.; Sakurada, A.; Nakamura, S.; Teruya, S.; Koga, O.; Hori, Y. Infrared Reflection Absorption Spectroscopy of Sulfuric Acid Anion Adsorbed on Stepped Surfaces of Platinum Single-Crystal Electrodes. *Journal of Physical Chemistry B* **2002**, *106* (8), 1985–1990. <https://doi.org/10.1021/jp012456o>.

(48) Zhang, I. Y.; Zwaschka, G.; Wang, Z.; Wolf, M.; Campen, R. K.; Tong, Y. Resolving the Chemical Identity of H₂SO₄ Derived Anions on Pt(111) Electrodes: They're Sulfate. *Physical Chemistry Chemical Physics* **2019**, *21* (35), 19147–19152. <https://doi.org/10.1039/c9cp03397a>.

(49) Gossenberger, F.; Juarez, F.; Groß, A. Sulfate, Bisulfate, and Hydrogen Co-Adsorption on Pt(111) and Au(111) in an Electrochemical Environment. *Front Chem* **2020**, *8*. [View Article Online](https://doi.org/10.3389/fchem.2020.00634)
[DOI: 10.3389/fchem.2020.00634](https://doi.org/10.3389/fchem.2020.00634)

(50) Groppe, E.; Rojas-Buzo, S.; Bordiga, S. The Role of In Situ/Operando IR Spectroscopy in Unraveling Adsorbate-Induced Structural Changes in Heterogeneous Catalysis. *Chemical Reviews. American Chemical Society* **2023**, pp 12135–12169.
<https://doi.org/10.1021/acs.chemrev.3c00372>.

(51) Xia, Y.; Nelli, D.; Ferrando, R.; Yuan, J.; Li, Z. Y. Shape Control of Size-Selected Naked Platinum Nanocrystals. *Nat Commun* **2021**, *12* (1). <https://doi.org/10.1038/s41467-021-23305-7>.

(52) Lee, H.; Habas, S. E.; Kвесkin, S.; Butcher, D.; Somorjai, G. A.; Yang, P. Morphological Control of Catalytically Active Platinum Nanocrystals. *Angewandte Chemie - International Edition* **2006**, *45* (46), 7824–7828. <https://doi.org/10.1002/anie.200603068>.

(53) Yeh, K. Y.; Restaino, N. A.; Esopi, M. R.; Maranas, J. K.; Janik, M. J. The Adsorption of Bisulfate and Sulfate Anions over a Pt(1 1 1) Electrode: A First Principle Study of Adsorption Configurations, Vibrational Frequencies and Linear Sweep Voltammogram Simulations. *Catal Today* **2013**, *202* (1), 20–35. <https://doi.org/10.1016/j.cattod.2012.03.011>.

(54) Chen, C. H.; Halford, A.; Walker, M.; Brennan, C.; Lai, S. C. S.; Fermin, D. J.; Unwin, P. R.; Rodriguez, P. Electrochemical Characterization and Regeneration of Sulfur Poisoned Pt Catalysts in Aqueous Media. *Journal of Electroanalytical Chemistry* **2018**, *816*, 138–148. <https://doi.org/10.1016/j.jelechem.2018.03.015>.

(55) Smirnov, M. Y.; Kalinkin, A. V.; Pashis, A. V.; Prosvirin, I. P.; Bukhtiyarov, V. I. Interaction of SO₂ with Pt Model Supported Catalysts Studied by XPS. *Journal of Physical Chemistry C* **2014**, *118* (38), 22120–22135. <https://doi.org/10.1021/jp5069126>.

(56) Aoki, M.; Shishido, T.; Morooka, T.; Nakanishi, T.; Masuda, T. Electrochemical Oxidative Desorption of Adsorbed Sulfur Species on (111) Surfaces of Single Crystals of Pure Pt and Pt-Based Bimetallic Alloys. *Journal of Physical Chemistry C* **2025**, *129* (4), 2122–2131. <https://doi.org/10.1021/acs.jpcc.4c06652>.

(57) Lee, A. F.; Wilson, K. Sulfate-Enhanced Catalytic Destruction of 1,1,1-Trichlorethane over Pt(111). *Journal of Physical Chemistry B* **2006**, *110* (2), 907–913. <https://doi.org/10.1021/jp054658g>.

(58) Chen, C. H.; Halford, A.; Walker, M.; Brennan, C.; Lai, S. C. S.; Fermin, D. J.; Unwin, P. R.; Rodriguez, P. Electrochemical Characterization and Regeneration of Sulfur Poisoned Pt Catalysts in Aqueous Media. *Journal of Electroanalytical Chemistry* **2018**, *816*, 138–148. <https://doi.org/10.1016/j.jelechem.2018.03.015>.



Data Availability Statement

The datasets supporting this article, titled "IR Nanospectroscopy Mapping of Facet-Dependent Sulfur Poisoning and Thermal Regeneration on Platinum Nanocrystals" are openly available on Zenodo and can be accessed via the DOI: 10.5281/zenodo.17778202.

